Heterogeneous to homogeneous melting transition visualized with ultrafast electron diffraction

M. Z. Mo,[1*†] Z. Chen,[1†] R. K. Li,[1] M. Dunning,[1] B. B. L. Witte,[1,2] K. Baldwin,[3] L. B. Fletcher,[1] J. Kim,[1] A. Ng,[4] R. Redmer,[2] A. H. Reid,[1] P. Shekhar,[5] X. Z. Shen,[1] M. Shen,[5] K. Sokolowski-Tinten,[6] Y. Y. Tsui,[5] Y. Q. Wang,[3] Q. Zheng,[1] X. J. Wang,[1] S. H. Glenzer[1*]

[1]SLAC National Accelerator Laboratory, Menlo Park, California 94025, USA

[2]Institut für Physik, Universität Rostock, 18051 Rostock, Germany

[3]Los Alamos National Laboratory, Bikini Atoll Road, Los Alamos, NM 87545, USA

[4]Department of Physics and Astronomy, University of British Columbia, Vancouver, BC V6T 1Z1 Canada

[5]Department of Electrical and Computer Engineering, University of Alberta, Edmonton, AB T6G 2V4, Canada

[6]Faculty of Physics and Centre for Nanointegration Duisburg-Essen, University of Duisburg-Essen, Lotharstrasse 1, D-47048 Duisburg, Germany

[†] Contributed equally to this work

[*]To whom correspondence should be addressed; E-mail: mmo09@slac.stanford.edu, glenzer@slac.stanford.edu

The ultrafast laser excitation of matters leads to non-equilibrium states with complex solid-liquid phase transition dynamics. We used electron diffraction at mega-electronvolt energies to visualize the ultrafast melting of gold on the atomic scale length. For energy densities approaching the irreversible melting regime, we first observed heterogeneous melting on time scales of 100 ps to 1000 ps, transitioning to homogeneous melting that occurs catastrophically

This material is based upon work supported by the U.S. Department of Energy, Office of Science, under Contract No. DE-AC02-76SF00515.

within 10-20 ps at higher energy densities. We showed evidence for the heterogeneous coexistence of solid and liquid. We determined the ion and electron temperature evolution and found superheated conditions. Our results constrain the electron-ion coupling rate, determine the Debye temperature and reveal the melting sensitivity to nucleation seeds.

One-sentence summary: The first observation of heterogeneous melting has tested molecular dynamics simulations and revealed the sensitivity to nucleation seeds for melting.

Modern ultrafast laser techniques can bring materials into states far from thermal equilibrium. These ultrafast processes yield extreme material conditions with thermal energy comparable to the Fermi energy and the ion-ion coupling parameter exceeding unity, referred to as warm dense matter (*1, 2*). These conditions exist as a transient state in a variety of processes ranging from laser micromachining (*3*) to inertial confinement fusion experiments (*4*).

In the case of semiconductors, ultrafast optical irradiation can cause strong bond softening and non-thermal melting owing to the changes in the potential-energy surface of the lattice by the excited valence electrons (*5, 6*). In contrast, melting of metals is a purely thermal process governed by the energy coupling between the excited electrons and relatively cold lattices (*7, 8*). Two-temperature modeling coupled to Molecular Dynamics (TTM-MD) simulations predicted the existence of distinct melting regimes in ultrafast laser excited gold (*9*). At low energy densities, the simulations predict that the slow ion heating rate allows the solid-liquid phase transition to occur as heterogeneous melting initiated on liquid nucleation sites on surfaces, grain boundaries, or defects, resulting in a slow melting process limited by the subsonic melt-front propagation speed. However, higher energy densities can cause extremely high heating rates exceeding 10^{14} K/s, producing a superheated state where homogeneous nucleation occurs catastrophically throughout the sample. Early electron-diffraction experiments observed long

melt times in Al, but did not observe the heterogeneous coexistence (*10*). Other experiments were performed in the homogeneous melting regime (*7, 8, 11, 12*), but determining melt times and testing theoretical predictions (*9, 13–15*) have been elusive. In addition, whether the highly excited electron system can cause bond hardening (*8, 16*) or softening (*17*) in gold remains controversial, further complicating the understanding of ultrafast laser-induced solid-liquid phase transitions in metals.

Visualizing solid-liquid phase transitions and accurately measuring melt times in the heterogeneous and homogeneous melting regimes required the development of ultrafast electron diffraction (UED) with MeV energies (*18–20*). Due to reduced space charge effect, this device provides high peak currents ($\sim$100 mA), enabling measurements with extremely high signal-to-noise ratios. The electron beam is produced by ultrafast ultraviolet laser irradiation of a copper cathode and accelerated by a linac accelerator-type RF gun; the same laser is split off to heat the sample, providing accurate cross timing between laser pump and the electron probe of < 30 fs (rms) (*21, 22*). Furthermore, MeV electrons form a nearly flat Ewald sphere on the reciprocal space allowing simultaneous access to multiple orders of diffraction peaks (*23*). Finally, multiple elastic scattering effects are less probable in nanometer thin films at these energies due to their relatively large elastic mean-free-path (*24*).

We employed 35-nm-thick 100-oriented single-crystalline (SC) or 30-nm-thick polycrystalline (PC) gold foils for the electron diffraction measurements. We uniformly excited these freestanding foils by 130 fs (FWHM), 400 nm laser pulses at 4^o incidence angle with flat-top-like intensity profiles of $\sim$ 420 μm diameters. The root-mean-square intensity variation of the optical pump within the probed area is better than 5%, ensuring uniform excitations in the transverse direction. We expect uniform heating in longitudinal direction due to the ballistic energy transport from non-thermal electrons excited by the laser pulses (*12, 25, 26*). We performed time-resolved electron diffraction measurements in normal incidence transmission geometry

with 3.2 MeV electrons. We focused these relativistic electron bunches onto the target with diameters of $\sim 120\ \mu m$ (FWHM), bunch charges of ~ 20 fC and pulse durations of ~ 350 fs (FWHM) (*22*).

We show three distinct melting regimes of the laser-excited SC gold with raw diffraction patterns measured at various delay times for three selective absorbed energy densities ϵ (Fig. 1). At the highest energy density of 1.17 MJ/kg (Figs.1 A-D), we first observed the decrease of Laue diffraction peaks (LDP) intensity due to the Debye-Waller effect immediately after laser excitation. At 2 ps delay, the heights of diffraction peaks relative to the adjacent backgrounds show obvious drops compared to the reference data taken before the arrival of the laser pulse (-2 ps) (Fig.1 D). At 7 ps delay, the data shows a weak liquid diffraction ring, a signature of the formation of a disorderd state. At 17 ps, the complete disappearance of the LDPs and the appearance of the two liquid Debye-Scherrer rings demonstrate that the sample is completely molten. Such fast melting process is indicative of homogeneous melting according to molecular dynamics simulations (*9, 27*).

At intermediate energy density of 0.36 MJ/kg (Figs.1 E-H), the low order LDPs from regions of solid gold and the primary diffraction ring from liquid gold are simultaneously visible at the delay time of 20 ps. Such heterogeneous coexistence persists over long time scales until 800 ps delay, long after electron-ion equilibration time of $\sim$50 ps, demonstrating the solid-liquid coexistence at heterogeneous melting conditions.

At even lower energy density of 0.18 MJ/kg (Figs.1 I-L), the data show strong LDPs over longer duration even at 100 ps when ion temperature T_i should have reached its apex, but the melt front is propagating at a very slow rate. At 1000 ps, the sample is still in a solid-liquid co-existence regime, and it does not show complete disappearance of solid diffraction peaks even at delay times as large as 3000 ps. We categorized this case as incomplete melting regime because the energy density deposited in the sample is below the requirement of complete melting

expected at ~ 0.22 MJ/kg (*28*).

Our experiment provided high-quality liquid diffraction data spanning over a large reciprocal space that allowed us to determine its corresponding ion temperature. We realized this by comparing with the theoretical liquid scattering signal based on DFT-MD simulations (*23*). We employed this analysis for $\epsilon = 1.17$ MJ/kg, which yields a best fit $T_i = 3500\,K \pm 500\,K$ at the delay time of 17 ps, indicating a superheated state. The error bar represents one standard deviation uncertainty.

We characterized the initial and final temperatures of the dynamic melting process and thus the electron-ion coupling rate g_{ei} is constrained with a pair of coupled equations of the commonly used two-temperature model (TTM) to describe the temperature evolution of both electron and ion subsystems in ultrafast laser excited materials (*23*). We used the temperature-dependent electron and ion specific heat $C_e(T_e)$ and $C_i(T_i)$ of gold from Refs. (*29*) and (*30*) respectively. To first order, we assumed a temporally constant g_{ei} and determined its value by solving for the ion temperature at complete melt, taking into account the energy consumed by latent heat. The TTM yields $g_{ei} = (4.9 \pm 1) \times 10^{16}\,W/m^3/K$ at 1.17 MJ/kg. We compared the temporal evolution of T_e and T_i using this value for g_{ei} with those based on simulated T_e-dependent values for g_{ei} from Ref. (*29*) at 1.17 MJ/kg (Fig.2 D). We found that T_e-dependent g_{ei} overestimates the ion temperature at complete melting by more than 60%.

We estimated the temporal evolution of the Debye temperature Θ_D (*23*), a manifestation of interatomic potential (*16*), directly from the measured LDP decay using T_i determined from the TTM. We observed rapid decay of Θ_D (Fig.2 G-I). This differs dramatically from both the bond-hardening model based on the T_e-dependent phonon spectrum in non-equilibrium conditions (*16*), and those values employed in Ref. (*8*). Neither of these models agreed with our measured (220) LDP decay (Figs. 2 A-C). Below the nominal melting temperature ($T_{melt}^{nom} = 1340\,K$), Θ_D showed striking agreement with the X-ray measurements of gold under thermal equilibrium

(*31*), suggesting that T_i is still the dominant factor for Θ_D in non-equilibrium gold at much higher T_e. Our finding is thus different from the previously reported bond-softening model of gold (*17*), which ascribed the effect to the highly elevated T_e.

We arrived at the following picture for ultrafast melting of gold. We fit our entire data set over three melting regimes with only one single assumption that g_{ei} is weakly dependent on energy density, modestly increasing from $2.2 \times 10^{16}\, W/m^3/K$ at the lowest energy density to $4.9 \times 10^{16}\, W/m^3/K$ for the highest energy density. For example, using $g_{ei} = 2.2 \times 10^{16}\, W/m^3/K$ for the lowest energy density from Ref. (*26*), leads to Debye temperature decay consistent with X-ray measurements at equilibrium conditions (Fig. 2I). For the heterogeneous melting regime, we linearly interpolated g_{ei} as a function of energy density between 0.18 MJ/kg and 1.17 MJ/kg, resulting in g_{ei}=$2.7\times10^{16}\, W/m^3/K$ at 0.36 MJ/kg. This value for g_{ei} yields Θ_D also consistent with data from Ref. (*31*) below T_{melt}^{nom} (Fig. 2H).

An important observable to quantify the lattice dynamics in laser-induced melting processes is the complete melting time, τ_{melt}, corresponding to the duration over which the long-range order is completely lost after laser arrival. We identified τ_{melt} by the complete disappearance of (200) diffraction peaks, whose intensity is most resistant to thermal vibrations and disordering effects, together with appearance of the two broad peaks of the liquid structure factor. For comparison, we also measured the complete melting time for the 30-nm-thick PC gold thin films. Both SC and PC samples show similar trends for τ_{melt} (Fig. 3). As energy density decreased, τ_{melt} first exhibits a gentle increase but then rises dramatically by orders of magnitude as energy density drops below ~ 0.4 MJ/kg. The complete melting threshold was found at ~ 0.25 MJ/kg, similar to the expected value of ~ 0.22 MJ/kg (*28*). We attributed the observed different characteristic time scales of τ_{melt} to homogeneous melting and heterogeneous melting, the two mechanisms of ultrafast melting. TTM-MD simulations (*9, 27, 32*) showed that the maximum velocity of melt front propagation is below 15% of the sound speed (∼500 m/s for gold), above

which homogeneous liquid nucleation dominates the melting process. Using this estimate suggests a minimum expected time for completion of the heterogeneous melting of 45 ps, including the time to reach T_{melt}^{nom} ($\sim$10 ps). This estimation agrees with our observation of the transition between the two melting mechanisms.

Quantitatively, in the heterogeneous melting regime, our PC results are consistent with electron diffraction measurements of Refs. (*33, 34*) and indicate a shorter melting time than SC samples. We can explain this by the increased liquid nucleation seeds at grain boundaries of nanocrystalline structures and the additional crystal defects in PC samples (*28*). The nucleation seed density in PC samples can be estimated with the measured τ_{melt} and calculated melt front velocities (*10*). For example, in the case of 0.28 MJ/kg, it takes $\sim$ 20 ps to reach T_{melt}^{nom}, but complete melting occurs at 130 ps. Combining this observation with melt front velocities ranging from 150 m/s to 300 m/s (*35*), results in an average distance between nucleation seeds ranging from 35 nm to 70 nm, corresponding to a nucleation seed density ranging from 1×10^4 μm^{-3} to 7×10^4 μm^{-3}.

Our data from SC samples showed functional agreement with the TTM-MD simulation results of SC gold by Lin $et\ al.$ (*9*) and Mazevet $et\ al.$ (*13*). However, the threshold of the transition between heterogeneous melting and homogeneous melting was found to be higher than predicted (*9*). We speculate this could be in large part due to the EAM potential employed in the simulations, i.e. the resultant melting temperature is 963 K, and the threshold for complete melting is 0.13 MJ/kg, both of which are much lower than experimental observations. Meanwhile, for homogeneous melting the slightly lower τ_{melt} calculated from Mazevet's simulations could be due to the fact that the thin film geometry was not considered. Moreover, in the TTM part of both simulations: (i) a simple free electron gas model based electron heat capacity was used, which was found to overestimate T_e (*36*), and (ii) the electron-ion coupling rate was set to the value consistent with low-temperature incomplete melting conditions.

Previous MD simulations correctly predicted the existence of the transition between the heterogeneous and homogeneous melting regimes, as shown with our experiments. However, our data reveals missing physical phenomena that will need to be included in the modeling of ultrafast melting dynamics. The observation of heterogeneous coexistence is significant because it reveals a novel method for addressing important questions related to the determination of nucleation seeds for melting. This will provide critical information to test and improve the kinetic theories of melting, and advance the material processing related to solid-liquid phase transition to atomic level precision.

References and Notes

1. S. Ichimaru, *Rev. Mod. Phys.* **54**, 1017 (1982).

2. A. Kritcher, et al., *Science* **322**, 69 (2008).

3. R. R. Gattass, et al., *Nature Photonics* **2**, 219 (2008).

4. S. H. Glenzer, et al., *Science* **327**, 1228 (2010).

5. C. W. Siders, et al, *Science* **286**, 1340 (1999).

6. M. Harb, et al, *Phys. Rev. Lett.* **100**, 155504 (2008).

7. B. J. Siwick, et al, *Science* **302**, 1382 (2003).

8. R. Ernstorfer, et al, *Science* **323**, 1033 (2009).

9. Z. Lin, et al, *Phys. Rev. B* **73**, 184113 (2006).

10. S. Williamson, et al., *Phys. Rev. Lett.* **52**, 2365 (1984).

11. T. Ao, et al, *Phys. Rev. Lett.* **96**, 055001 (2006).

12. Z. Chen, et al., *Phys. Rev. Lett.* **108**, 165001 (2012).

13. S. Mazevet, et al., *Phys. Rev. Lett.* **95**, 085002 (2005).

14. K. Lu, et al., *Phys. Rev. Lett.* **80**, 4474 (1998).

15. B. Rethfeld, et al., *Phys. Rev. B* **65**, 092103 (2002).

16. V. Recoules, et al, *Phys. Rev. Lett.* **96**, 055503 (2006).

17. S. L. Daraszewicz, et al, *Phys. Rev. B* **88**, 184101 (2013).

18. X. J. Wang, et al., *J. Korean Phys. Soc.* **48**, 390 (2006).

19. J. B. Hastings, *et al.*, *Appl. Phys. Lett.* **89**, 184109 (2006).

20. R. Li, *et al.*, *Rev. Sci. Instrum.* **80**, 083303 (2009).

21. S. P. Weathersby, et al, *Rev. Sci. Instrum.* **86**, 073702 (2015).

22. M. Z. Mo, et al., *Rev. Sci. Instrum.* **87**, 11D810 (2016).

23. See supporting online materials .

24. P. Musumeci, et al., *Appl. Phys. Lett.* **97**, 063502 (2010).

25. S. D. Brorson, et al., *Phys. Rev. Lett.* **59**, 1962 (1987).

26. J. Hohlfeld, et al., *Chem. Phys.* **251**, 237 (2000).

27. D. S. Ivanov, et al., *Phys. Rev. B* **68**, 064114 (2003).

28. Z. Lin, et al., *J. Phys. Chem. C* **114**, 5686 (2010).

29. Z. Lin, L. V. Zhigilei, *Phys. Rev. B* **77**, 075133 (2008).

30. G. Cordoba, et al., *Phys. Stat. Sol. (a)* **6**, 581 (1971).

31. V. Synecek, et al., *Acta Cryst.* **A26**, 108 (1970).

32. D. Ivanov, et al., *Phys. Rev. Lett.* **98**, 195701 (2007).

33. J. R. Dwyer, et al., *Philos. Trans. R. Soc. London, Ser. A* **364**, 741 (2006).

34. J. R. Dwyer, et al., *J. Mod. Opt.* **54**, 905 (2007).

35. F. Celestini, et al., *Phys. Rev. E* **64**, 041605 (2002).

36. B. Holst, et al., *Phys. Rev. B* **90**, 035121 (2014).

37. A. Kossoy, et al., *Adv. Optical. Mater* **3**, 71 (2015).

38. R. Powell, et al., *Thermal conductivity of selected materials* (National standard reference data series, 1966).

39. Y. Wang, et al, *J. Appl. Phys* **119**, 225109 (2016).

40. E. A. Brandes, *Smithells Metal Reference Book, 6th ed.* (Butterworths, London, 1983).

41. J. P. Perdew, et al, *Phys. Rev. Lett.* **77**, 3865 (1996).

42. G. Kresse, et al, *Phys. Rev. B* **47**, 558 (1993).

43. P. E. Blöchl, et al, *Phys. Rev. B* **50**, 17953 (1994).

44. G. Kresse, et al, *Phys. Rev. B* **59**, 1758 (1999).

45. S. Nosé, *J. Chem. Phys.* **81**, 511 (1984).

46. Y. Waseda, *The Structure of Non-Crystalline Materials* (McGraw-Hill, New York, 1980).

47. P. Doyle, et al, *Acta Cryst.* **A24**, 390 (1968).

48. P. Johnson, et al, *Phys. Rev. B* **6**, 4370 (1972).

49. V. Vlcek, et al, *Phys. Rev. B* **85**, 184201 (2012).

50. A. Ng, et al, *Phys. Rev. B* **94**, 033213 (2016).

Acknowledgments

We would like to thank SLAC management for the strong support. The technical support by SLAC Accelerator Directorate, Technology Innovation Directorate, LCLS Laser Science $\&$ Technology Division and Test Facilities Department is gratefully acknowledged. We would also like to thank the technical support on sample manufacturing from the Center for Integrated Nanotechnologies, a DOE nanoscience user facility jointly operated by Los Alamos and Sandia National Laboratories. This work was supported by the U.S. Department of Energy Contract No. DE-AC02-76SF00515 and the DOE Fusion Energy Sciences under FWP $\#$100182, and partially supported by DOE BES Accelerator and Detector $R\&D$ program, the SLAC UED/UEM Initiative Program Development Fund. The support from Natural Sciences and Engineering Research Council of Canada is also acknowledged. K.S.T. acknowledges financial support from the German Research Council through project C01 "Structural Dynamics in Impulsively Excited Nanostructures" of the Collaborative Research Center SFB 1242 "Non-Equilibrium Dynamics of Condensed Matter in the Time Domain. All data and analysis details presented in this work are available upon request to M. M..

Supplementary materials

Materials and Methods

Supplementary Text

References (37 - 50)

Figs. S1 to S9

Movies S1 to S3

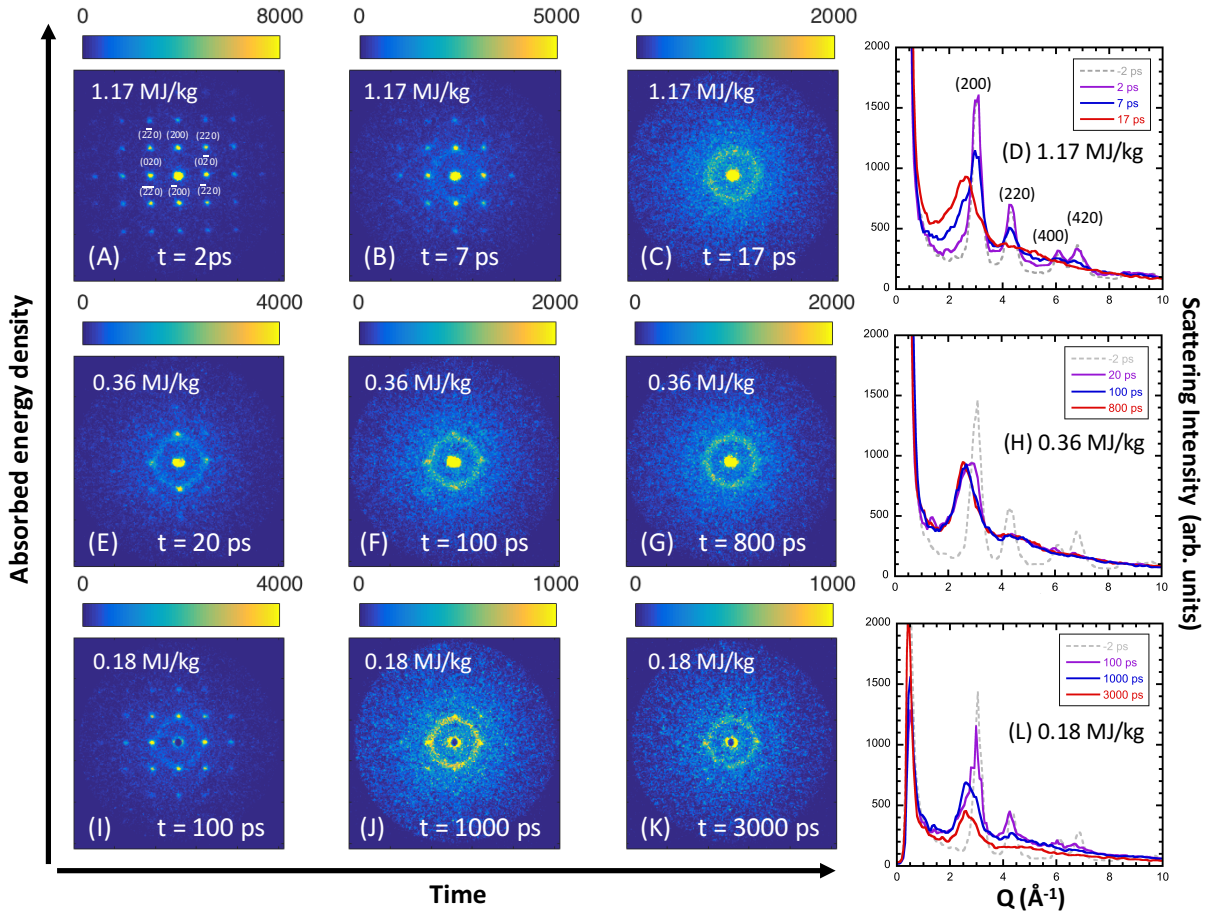

Figure 1: MeV electron diffraction studies of the ultrafast solid-liquid phase transition in single-crystalline Au. (A) - (C) Snapshots of the raw diffraction patterns at selective pump-probe delay times for homogeneous melting at ϵ = 1.17 MJ/kg; (E)-(G) Heterogeneous melting at ϵ = 0.36 MJ/kg ; (I)-(K) Incomplete melting at ϵ = 0.18 MJ/kg. The radially averaged lineouts of the displayed diffraction patterns together with the reference lineouts taken at negative delay are shown in (D), (H) and (L) for these different energy densities respectively. The color bars represent the scattering intensity in arbitrary units.

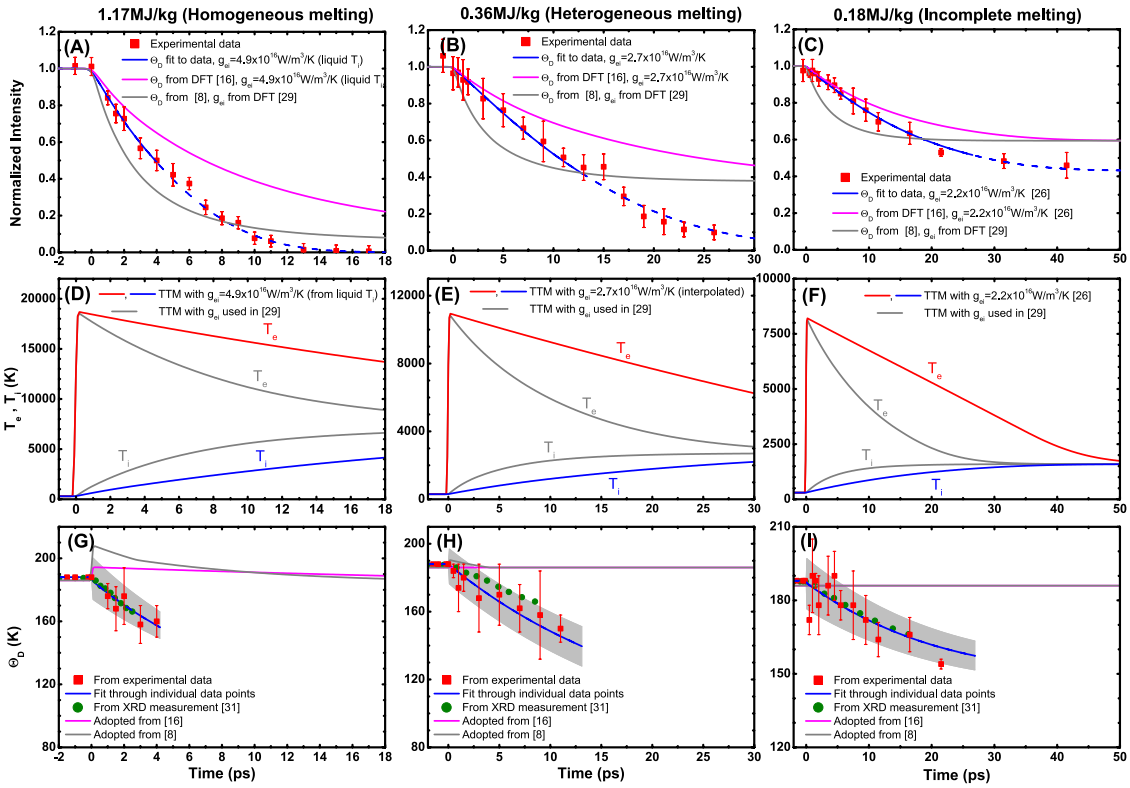

Figure 2: Energy density dependence of the lattice heating and disordering process. (A) - (C) experimental data of (220) decay (red solid squares) at different excitation energy densities, compared with three different models to calculate Debye-Waller factor (23): $\Theta_D(T_i)$ derived from (220) decay with constant g_{ei} (blue solid and dashed lines), $\Theta_D(T_e)$ from Ref. (*16*) with constant g_{ei} (magenta line), and $\Theta_D(T_e)$ used in Ref. (*8*) with g_{ei} from DFT calculations (*9*) (gray line). The (220) intensities were normalized with respect to those values from the laser-off diffraction pattern of the same sample. The error bars represent one standard deviation (SD) uncertainties. (D) - (F) temporal evolution of T_e and T_i simulated by TTM with different g_{ei} at energy densities corresponding to data of (A) - (C). (G) - (I) temporal evolution of Θ_D ($\pm$SD) derived from the experimental (220) decay (red squares) up to T_{melt}^{nom}, and the linear fit through individual data points as a function of T_i (blue solid line with the gray area representing error bar ($\pm$SD)), which are compared with the X-ray measurements at equilibrium conditions from Ref. (*31*), shown by the green dots, the DFT calculations from Ref. (*16*), shown by the magenta line, and results adopted from Ref. (*8*), shown by the gray line. In (A)-(C), the solid blue lines represent the data determined below the nominal T_{melt}^{nom} of 1340 K, and the dashed lines represent Debye-Waller factor based on linearly extrapolated Θ_D as a function of T_i.

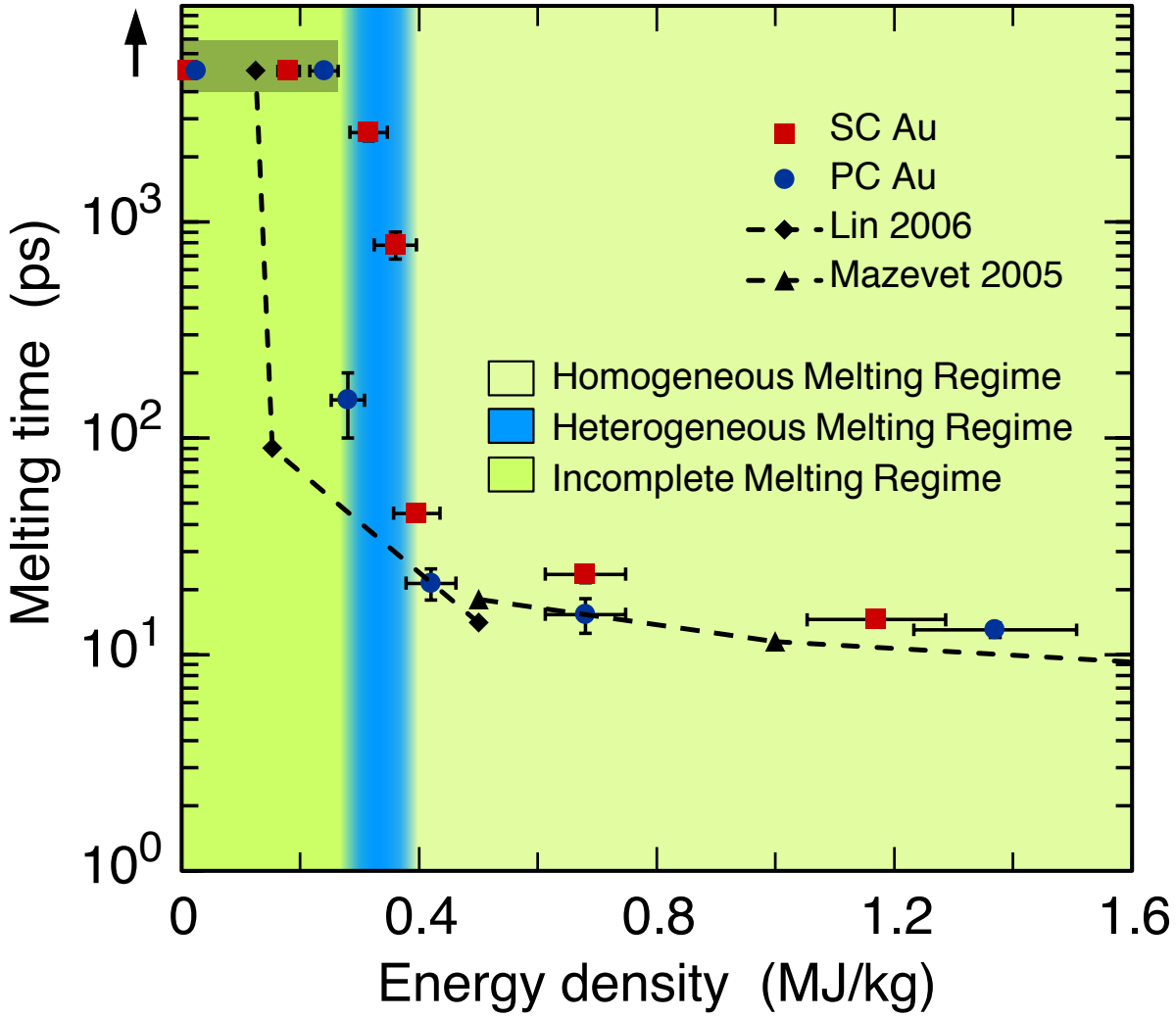

Figure 3: Energy density dependence of ultrafast-laser-induced melting mechanisms in Au. The measured melting time of SC Au and PC Au are represented by red squares and blue circles respectively, as compared with TTM-MD simulation by Lin *et al.* (*9*) and Mazevet *et al.* (*13*). The vertical error bars are given by the time step intervals around the observed melting times, while the horizontal error bars represent one standard deviation uncertainty of the measured absorbed energy density. Three melting regimes, i.e. homogeneous, heterogeneous and incomplete melting, are identified from the measurements and indicated by the various background colors. Note the data located inside the gray shaded area are beyond the instrument limit of 3 ns for our experiments, and the two data points on the left are from measurements of below damage threshold.